# AERODYNAMIC CHARACTERISTICS OF THE FLAT PLATE AIRFOIL AT LOW REYNOLDS NUMBERS

by

Hansong Liu

A thesis submitted to The Johns Hopkins University in conformity with the requirements for the degree of Master of Science.

Baltimore, Maryland

May, 2021

# Abstract

In order to provide a better understanding on unsteady flow and the aerodynamic characteristics of the flat plate airfoil, a computational study has been performed to investigate the flow structures and performance at the low Reynolds number $O(10^2 \sim 10^3)$ regime. Using a highly resolved, sharp interface immersed boundary method to simulate incompressible viscous flow past a stationary two-dimensional flat plate, we found that depending on the combination of angle of attack ($AOA$) and Reynolds ($Re$) number, the flow structures can be classified into one of the following categories: 2S, 2P, 1S+1P, and P, where S and P represent 'a single vortex' and 'a vortex pair' respectively. The performance of the flat plate airfoil, quantified as lift over drag ($C_L/C_D$), is shown to be the most efficient at ultra low $Re$ numbers among the several airfoil shapes being compared to.

**Primary Reader and Advisor:** Jung-Hee Seo

**Secondary Reader:** Rajat Mittal

# Contents

# List of Tables

# List of Figures

# Chapter 1

# Introduction

The study of lift and drag forces has occupied a fundamental place in fluid dynamics. As early as in the 18th century, Isaac Newton developed a theory of fluid resistance, noticing the effects of friction and viscosity. Later Navier and Stokes developed equations describing flow of incompressible fluids, extending the work by Leonhard Euler. On the other hand, Wilbur and Orville Wright measured their own aerodynamic data with a series of wind tunnel tests. They made the first successful powered flight in December 1903. More recent studies concerning fluid mechanics are in the higher Reynolds-number range of $O(10^6)$, which is closely related to the development of larger and/or faster airplanes over the past century. Some early collections of airfoil data are made available by Carmichael and Erikson (1981) [6], and Miley (1982) [24]. Although our knowledge on these high $Re$ is quite extensive, the research on flow

at low $Re$ numbers is largely insufficient. With growing interest in small-scale Unmanned Aerial Vehicle (UVA), and Micro Air Vehicle (MAV), the need for better understanding the aerodynamics at lower $Re$ numbers is urgent. Some early studies on the lower $Re$ are conducted by Patrick, using 3 wind tunnels in England in 1971, and Bosco in Milano, Italy in 1972 [5]. Their studies are for a $Re$ number $\boldsymbol{O}(10^4 \sim 10^5)$. However, studies at ultra low $Re$ numbers are still lacking. In the current study, we examine the aerodynamic characteristics of a thin flat plate airfoil at chord based $Re$ numbers ranging from 500 to 2000. Fig.1.1 shows the variation of maximum sectional lift-to-drag ratio with the chord-based $Re$ number. it is noted that higher lift-to-drag ($C_L/C_D$) ratios are achieved at the higher $Re$ numbers. As a result most past research, which focused on optimization of an airfoil at its operating $Re$ number, such as thickness, aspect ratio, leading and trailing edge shapes, is not necessarily applicable for airfoils that operate at the low $Re$ range. Thus, one of the objectives of the current research is to compare the performance of a flat plate airfoil to other airfoils that are better suited for higher $Re$ number.

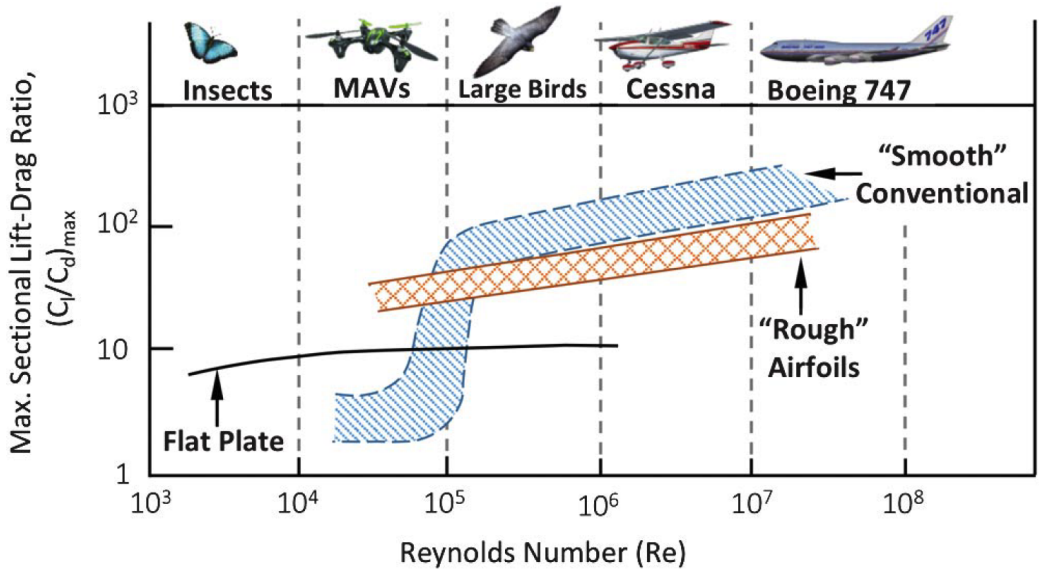


**Figure 1.1:** Effect of Reynolds number on airfoil maximum sectional lift-to-drag ratio from Winslow *et al.* [40]

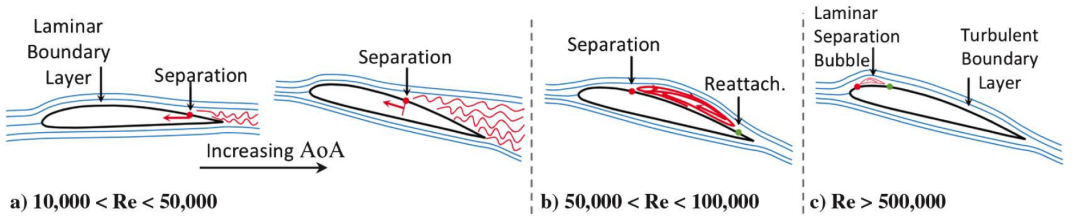


**Figure 1.2:** Illustration highlighting conventional airfoil separation characteristics at different Reynolds number regimes below $10^6$ from Winslow *et al.* [40]

## 1.1 High Reynolds Number Airfoil Aerodynamics

A schematic drawing of the streamlines at various $Re$ number is shown in Fig. 1.2. At a high $Re$ number as shown in Fig. 1.2 c ($\boldsymbol{Re} > 500,000$), the laminar flow separates as a result of adverse pressure gradient. After laminar separation occurs, turbulent boundary layer is caused by the backflow to the surface. The turbulent boundary layer is more reluctant to separate than laminar boundary layers due to the increased interchange of momentum form outer layers [1]. At lower Reynolds numbers as shown in Fig. 1.2 b ($50,000 < \boldsymbol{Re} < 100,000$), the separation bubble increases in size. Lowering the angle of attack or $Re$ number increases the length of the separation bubble as shown in Fig. 1.1. In either case, location of the separation bubble is extended in a direction closer to the trailing edge, while lower $Re$ number leads to the forward movement of separation point. At even lower $Re$ numbers as shown in a ($1000 < \boldsymbol{Re} < 50,000$), laminar separation occurs typically further down the tailing edge. The free shear layer after laminar separation normally fails to transition to turbulent flow in time to reattach to the airfoil surface [5]. Increasing in angle of attack moves the separation point towards the leading edge, and eventually causes sudden increase in drag and loss in lift, which is known as stall. The combination of small geometric scale and lower velocities

in this $Re$ number regime generates increasing importance of viscous effects compared to inertial effects. In addition to the inherent difficulty achieving such flow conditions in experiments, the distinctive characteristic of low $Re$ number introduces another common difficulty- measurements of data are very sensitive to boundary layer separation and reattachment. There is substantial record of non-repeatability of the early experiments on low-$Re$ airfoil [17]. Factors that affect the quality of the experiments include wind tunnel wall effects, variations from tunnels to tunnels, airfoil planform and so forth. Miley [24] observes more variation of the drag and lift coefficients in the NACA 4415 data, compared to the NACA 23012 data. Even the fundamental measurement of time-averaged $C_L$ ($C_D$) fails to converge as $Re$ drops below $10^5$ [36]. So far, we have seen $Re$ number of order $10^4$ and above.

**Table 1.1:** Table of separation point (SP), reattachment point (RP), and bubble length (BL) for present computations and McGhee et al. (noted as MWM); NR = not reported from Lin and Pauley [16]

| Reynolds no. | Angle of attack, deg | SP | RP | BL | $SP_{MWM}$ | $RP_{MWM}$ | $BL_{MWM}$ |
|---|---|---|---|---|---|---|---|
| $6 \times 10^4$ | 4 | 0.345 | 0.957 | 0.612 | NR | NR | NR |
| $1 \times 10^5$ | 4 | 0.355 | 0.762 | 0.407 | 0.35 | 0.73 | 0.38 |
| $2 \times 10^5$ | 4 | 0.407 | 0.662 | 0.255 | 0.40 | 0.62 | 0.22 |
| $1 \times 10^5$ | 0 | 0.452 | 0.885 | 0.433 | 0.45 | 0.87 | 0.42 |
| $1 \times 10^5$ | 7 | 0.288 | 0.635 | 0.347 | 0.32 | 0.56 | 0.24 |

## 1.2 Low Reynolds Number Airfoil Aerodynamics

Investigations on very low-$Re$ ($10^3$) aerodynamics ranges from ball sports, such as tennis and golf, to insect flyers, as well as special military aircrafts. The Reynolds number at which MAVs operate $\boldsymbol{O}(10^4)$ and will continue to decrease in the coming years [31]. In this $Re$ regime, considerably different flow patterns are expected, namely that the flow is laminar, viscously dominated and boundary layers are thicker, introducing frequent flow separation and unsteady vortex shedding. The distinctive property that the viscous effects are relatively large causes high drags and limits the maximum lift. From Fig. 1.1, we notice around a critical $Re = 10^5$, this performance transition takes place. Although biological flight mechanisms are abundant, there is little dedicated work on low-$Re$ airfoil aerodynamic research. Such deficiency arises from absence of suitable high-fidelity computational analysis methods, and difficulties in achieving accurate and repeatable experimental work. Nonetheless, general effects on performance of the geometry characteristics of airfoils at this $Re$ number are explored in literature, including variations in the thickness, camber, and leading/trailing edge shapes [14]. A number of computational modeling studies have been carried out for low-$Re$ airfoils in particular. Owing to the distinctive characteristics at low $Re$ number, studies cannot simply assume

the methodology successful at a high $Re$ is applicable to low-$Re$ cases. Some authors found that many successful aerodynamic codes, which were designed for the conventional $Re$ number, were not fit for the low-$Re$ range. Kunz and Kroo [13] used the IN2D code, which was originally developed at NASA Ames, based on an upwind finite differencing scheme. Their code inherited the features of steady models, which ignore the unsteady effects [13]. Mittal *et al.* [26] performed numerical simulations on NACA 0012 for different Reynold number using finite element formulation. They observed that the location of center of gravity of the airfoil is important in determining its pitch stability, but the tests are performed only at a single angle of attack. Ohmi *et al.* [28] studied vortex patterns for an oscillating and translating NACA 0012 airfoil for different angles of attack and angular amplitudes at $Re = 1500 \sim 10000$, noticing that the reduced frequency was the dominant parameter determining the markedly different characteristics of the unsteady vortices. However, they encounter some difficulties in isolating independent parameters and in reproducing the experiments due to the sensitivity to the experimental environment. Kurtulus [15] presented aerodynamic coefficients and vortex structures of NACA 0012 for many angles of attack at $Re = 1000$. In the study the onset of oscillatory behavior of aerodynamics forces, as well as unsteady vortex shedding at an $AOA$ of $8^\circ$ was observed. Hoarau *et al.* [10] showed for a NACA 0012 wing two-dimensional transition mechanisms to turbulence: that to aperiodicity beyond

the von Karman mode via a period-doubling scenario and the development of a shear-layer instability using direct numerical simulations (DNS). From Fig.

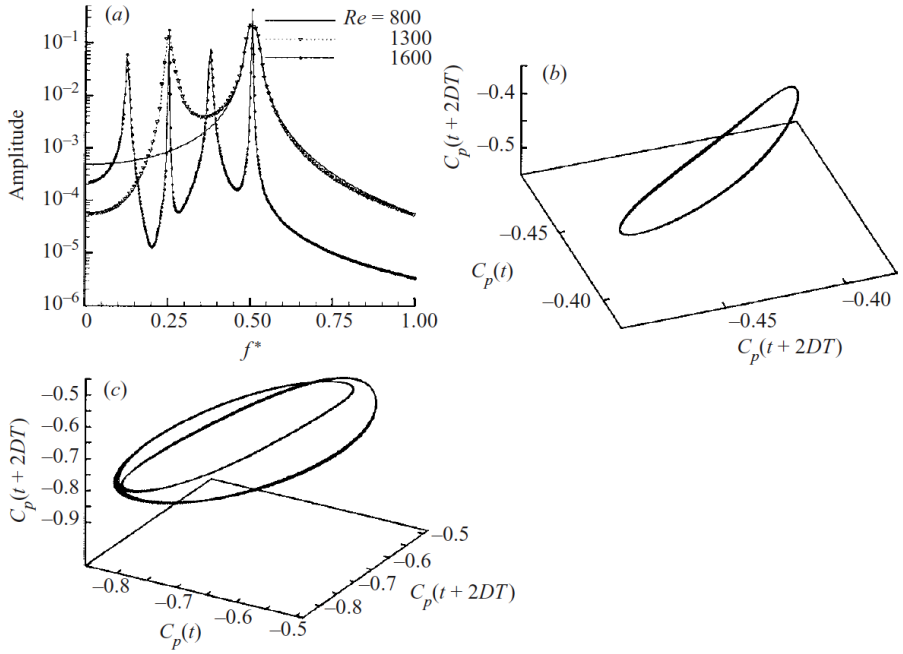


**Figure 1.3:** (a) Pressure coefficient spectra showing the period-doubling mechanism, and the corresponding attractors at (b) $Re = 800$ and (c) 1300 from HOARAU *et al.* [10]

1.3, we notice for increasing $Re$ number in the range $800 \sim 1600$, the obtained spectra of the pressure coefficient signals show a clear evolution of the von Karman instability and is related to a period-doubling scenario. Such phenomenon can be justified by the fact that the shed vortex close to the trailing edge is weakened at exactly $2T$ by the opposite vortex which starts being shed. Liu *et al.* [18] studied static and dynamic stalls, characterizing the nature of static stall to be a saddle-node bifurcation, involving hysteresis and jumping phenomena. In addition, dynamic stall was shown to have a variety of nonlinear phenomena, providing the basis for lift enhancement and drag reduction.

They propose an external excitation to enhance the lift and delay the static stall, which was tested to increase the time averaging lift by $80\%$ at $f = 1.6$, with at an initial $AOA$ of $20°$ and angular amplitude $15°$, in comparison with the static airfoil. However, only a single $Re$ was investigated there.

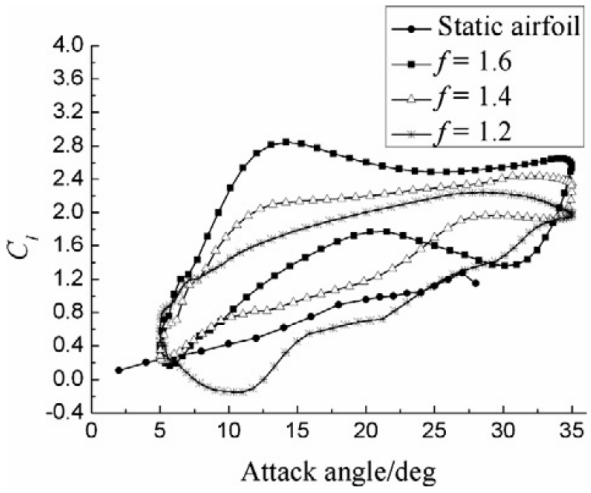


**Figure 1.4:** Diagrams of attack angle versus lift coefficient of dynamic and static airfoil ($\boldsymbol{Re = 1000, \alpha_0 = 20°, \alpha_{amp} = 15°}$) from Liu *et al* [18].

## 1.3 Flat Plate Airfoils at Low Reynolds Number

A flat plate is geometrically the simplest airfoil one can think of. In spite of its simplicity, its aerodynamic behavior can give significant values and implications to design and validation of computational or experimental models. A number of attempts have been carried out for the low-$Re$ flat plate airfoil

studies in the literature. For instance, Ahuja and Rowley [2] presented an algorithm for developing reduced-order models of the feedback control of high-dimensional linear unstable system. The algorithm was applied to control the two-dimensional flat plate at a large angle of attack at $Re = 100$, where the natural flow state is periodic vortex shedding. They placed the localized body force close to the trailing edge, for the model of linearized dynamics at angle of attack of 35°. However, the controllers they employed was only designated for a fixed set of parameters, such as $Re$ and $\alpha$.

A number of parameters, aspect ratio, angle of attack, and planform geometry, have been studied by Taira and Colonuis [35] for influence on the wake vortices and the resulting forces of three-dimensional flows over translated low-aspect-ratio flat plated at a $Re$ number of 300 and 500. They found that the tip vortices significantly influence the vortex dynamics and the forces on the wings. The flow at large convective times may reach a stable steady state, a periodic cycle or aperiodic shedding, depending on the aspect ratio, angle of attack and $Re$ number. For instance, Fig. 1.5 involves snapshots of two iso-surface visualization: the first is constant vorticity surface where $\omega_2 = 3$, shown in light gray; the second is the second invariant of the velocity gradient tensor ($\nabla u$), known as the Q-criterion, which is used to highlight the vortex cores, depicted by the dark gray surfaces ($Q = 3$). Positive Q-values give prominence to regions of high swirl in comparison to shear to represent coherent vortices [11]. It is

clear from the comparison that features of the initial transient stage lose their effect on the planform as flow is advected and diffused downstream, and thus the wake becomes strongly dependent on the aspect ratio value.

Although attempts have been made in modeling the flow past a low-$Re$ flat plate, the details on the full aerodynamic quantities of the flat plate are quite insufficient. Therefore, in the current study, we present the results from two-dimensional numerical simulations for a flow of $500 \leq Re = U_\infty C/\nu \leq 2000$, over a flat plate. A high resolution, unsteady incompressible Navier-Stokes simulation was performed, of which result serves to provide a database of time history of the aerodynamic coefficients, including force and moment coefficients, and center of pressure, plotted against angle of attack, for different $Re$ numbers. These data should come handy for reference for those that are interested in doing parallel work.

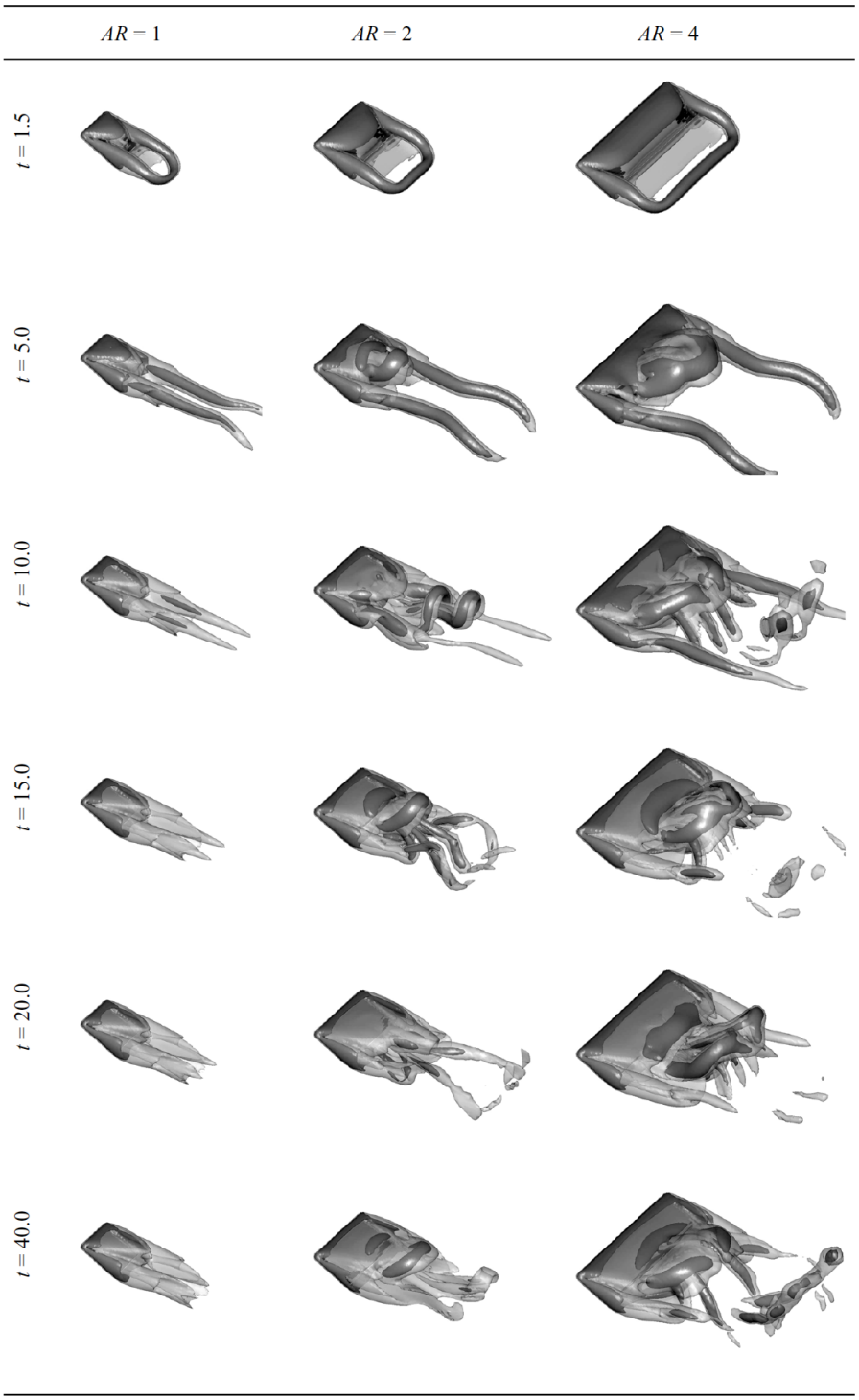


**Figure 1.5:** Top-port views of the wake vortices behind rectangular plates of $AR$ =1, 2 and 4 at $\alpha = 30^{\circ}$ and $Re$ =300. Shown are the iso-surface of $||\omega||_2$ =3 in light grey with vortex cores highlighted by the iso-surface of $Q$ =3 in dark grey from [35].

# Chapter 2

# Methodology

This section details the numerical flow solver, the specifics of numerical method, as well as the detailed parameters for the flat plate used to perform the simulations in the current study. The numerical flow solver employed in the study is 'ViCar3D', which stands for Viscous Cartesian Grid Solver for 3-D Immersed Boundaries. This sharp-interface immersed-boundary-method based solver was originally developed by Dr. Rajat Mittal and his research group over the years [25], [32]. This solver has been extensively used to simulate flows for a number of complex geometries using simple, non-conforming Cartesian girds [22], [33]. This is particularly useful as it features the advantage of not being constrained by complex boundaries or highly deformed grid cells [25]. The details of the flow solver and immersed boundary method have been mentioned in many existing works. However some important aspects, mostly

found in the work [25], which are not original to this work, are included for completeness.

## 2.1 ViCar3D Flow Solver

The governing equations considered here are the 2-D unsteady Navier-Stokes equations for a viscous incompressible flow with constant properties given by

$$\frac{\partial u_i}{\partial x_i} = 0 \tag{2.1}$$

$$\frac{\partial u_i}{\partial t} + \frac{\partial u_i u_j}{\partial x_j} = -\frac{1}{\rho}\frac{\partial p}{\partial x_i} + \nu \frac{\partial}{\partial x_j}\left(\frac{\partial u_i}{\partial x_j}\right) \tag{2.2}$$

where $i; j = 1; 2; 3$, $u_i$ are the velocity components, $p$ is the pressure, and where $\rho$ and $\nu$ are the fluid density and kinematic viscosity.

The Navier–Stokes Eqn. 2.2 are discretized using a cell-centered, collocated (non-staggered) arrangement of the primitive variables $(u_i, p)$. In addition to the cell-center velocities $(u_i)$, the face-center velocities, $(U_i)$, are computed see Fig. 2.1. The equations are integrated in time using the fractional step method of Van-Kan [38] which consists of three sub-steps. In the first sub-step of this method, a modified momentum equation is solved and an intermediate velocity $u^*$ obtained.Asecond-order, Adams–Bashforth scheme is employed for the

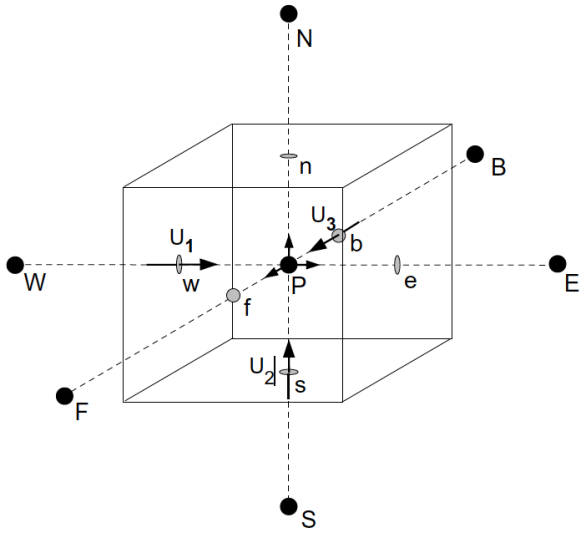


**Figure 2.1:** Schematic describing the naming convention and location of velocity components employed in the spatial discretization of the governing equations by Mittal *et al.* [25].

convective terms while the diffusion terms are discretized using an implicit Crank–Nicolson scheme which eliminates the viscous stability constraint. In this sub-step, the following modified momentum equation is solved at the cell-nodes

$$\frac{u_i^* - u_i^n}{\Delta t} + \frac{1}{2}[3N_i^n - N_i^{n-1}] = -\frac{1}{\rho}\frac{\delta p^n}{\delta x_i} + \frac{1}{2}(D_i^* + D_i^n) \tag{2.3}$$

where $N_i = \frac{\delta(U_j ui)}{\delta x_j}$ and $D_i = \nu \frac{\delta}{\delta x_j}\left(\frac{\delta u_i}{\delta x_j}\right)$ are the convective and diffusive terms respectively, and $\frac{\delta}{\delta x}$ corresponds to a second-order central difference. This equation is solved using a line-SOR scheme [3]. Subsequently, face-center velocities at this intermediate step $U^*$ are computed by averaging the corresponding values at the grid nodes. Similar to a fully staggered arrangement, only the face velocity component normal to the cell-face is calculated and used for computing

the volume flux from each cell. The following averaging procedure is followed:

$$\begin{aligned}
\tilde{u_i} &= u_i^* + \Delta t \frac{1}{\rho}\left(\frac{\delta p^n}{\delta x_i}\right)_{\text{cc}} \\
\tilde{U_1} &= \gamma_{\text{w}} \tilde{u_{1P}} + (1-\gamma_{\text{w}}) \tilde{u_{1W}} \\
\tilde{U_2} &= \gamma_{\text{s}} \tilde{u_{2P}} + (1-\gamma_{\text{s}}) \tilde{u_{2S}} \\
\tilde{U_3} &= \gamma_{\text{b}} \tilde{u_{1P}} + (1-\gamma_{\text{b}}) \tilde{u_{3B}} \\
U_i^* &= \tilde{u_i} - \delta t \frac{1}{\rho}\left(\frac{\delta p^n}{\delta x_i}\right)_{\text{fc}}
\end{aligned} \tag{2.4}$$

where $\gamma_w$, $\gamma s$ and $\gamma_b$ are the weights corresponding to linear interpolation for the west, south and back face velocity components respectively. Furthermore, cc and fc denote gradients computed at cell-centers and face-centers, respectively. The above procedure is necessary to eliminate odd–even decoupling that usually occurs with non-staggered methods and which leads to large pressure variations in space. The second sub-step requires the solution of the pressure correction equation

$$\frac{u^{n+1} - u_i^*}{\Delta t} = -\frac{1}{\rho}\frac{\delta p^{'}}{\delta x_i} \tag{2.5}$$

which is solved with the constraint that the final velocity $u_i^{n+1}$ be divergence-free. This gives the following Poisson equation for the pressure correction

$$\frac{1}{\rho}\frac{\delta}{\delta x_i}\left(\frac{\delta p^{'}}{\delta x_i}\right) = \frac{1}{\Delta t}\frac{\delta U_i^*}{\delta x_i} \tag{2.6}$$

and a Neumann boundary condition imposed on this pressure correction at all boundaries. This Poisson equation is solved with a highly efficient geometric multigrid method [4] which employs a Gauss–Siedel line-SOR smoother [30]. The ability to employ such methods is another key advantage of the current Cartesian grid approach over body-conformal unstructured grid approaches. Geometrical multigrid methods are relatively simple to implement and have very limited memory overhead. Furthermore, when coupled with powerful smoothers like line-Gauss–Siedel, they can lead to a numerical solution of the pressure Poisson equation which scales almost linearly with the number of grid points. In contrast, for unstructured body-conformal methods, one has to either resort to algebraic multigrid methods [20], [34] or other more complex methods such as agglomeration multigrid [19]. Another choice for solving the pressure Poisson equation would be Krylov subspace based methods (such as conjugate gradient or GMRES) but these require effective preconditioners to provide good performance. Our past experience with both stationary and non-stationary iterative methods [37], [41] indicates that geometric multigrid methods are very well suited for sharp interface immersed boundary methods and we have therefore used this method in the current solver. Once the pres-

sure correction is obtained, the pressure and velocity are updated as

$$
\begin{aligned}
p^{n+1} &= p^n + p^{'} \\
u_i^{n+1} &= u_i^* - \Delta t \frac{1}{\rho} \left( \frac{\delta p^{'}}{\delta x_i} \right)_{\text{cc}} \\
U_i^{n+1} &= U_i^* - \Delta t \frac{1}{\rho} \left( \frac{\delta p^{'}}{\delta x_i} \right)_{\text{fc}}
\end{aligned}
\tag{2.7}
$$

These separately updated face-velocities satisfy discrete mass-conservation to machine accuracy and use of these velocities in estimating the non-linear convective flux in Eq.2.3 leads to a more accurate and robust solution procedure. The advantage of separately computing the face-center velocities was initially proposed by Zang *et al.* [42] and discussed in the context of the Cartesian grid methods in Ye *et al.* [41]. The above collocated scheme is simpler to implement than a conventional staggered mesh scheme [42] and when coupled with a central-difference spatial scheme, it leads to a numerical discretization that has good discrete kinetic energy conservation properties [9] making it suitable and robust for simulating relatively high (up to at least $O(10^4)$) Reynolds number flows without the need for artificial dissipation or upwinding.

## 2.2 Numerical Method

The current immersed boundary method employs a multi-dimensional ghost-cell methodology to impose the boundary conditions on the immersed bound-

ary. The method proceeds by first identifying cells whose nodes are inside the solid boundary (termed "solid cells") and cells that are outside the body (termed "fluid cells"). The schematic in Fig. 2.2 shows the various types of cells for a 2D boundary cutting through a Cartesian grid. In order to accomplish this, we extend a line segment from the node of these cells into the fluid to an "image-point" (denoted by IP) such that it intersects normal to the immersed boundary and the boundary intercept (denoted by BI) is midway between the ghost-node and the image-point. Once the BI and the corresponding IP have been identified, a trilinear interpolant of the following form is used to express the value of a generic variable (say $\phi$) in the region between the eight nodes surrounding the image-point:

$$\phi(x_1, x_2, x_3) = C_1 x_1 x_2 x_3 + C_2 x_1 x_2 + C_3 x_2 x_3 + C_4 x_1 x_3 + C_5 x_1 + C_6 x_2 + C_7 x_3 + C_8 \quad (2.8)$$

The eight unknown coefficients can be determined in terms of the variable values of the eight surrounding nodes

$$\{C\} = [V]^{-1}\{\phi\} \quad (2.9)$$

where

$$\{C\}^T = \{C_1, C_2, C_3, ..., C_8\} \quad (2.10)$$

is the vector containing the eight unknown coefficients and

$$\{\phi\}^T = \{\phi_1, \phi_2, ..., \phi_8\} \tag{2.11}$$

are the values of the variables at the eight surrounding points. Furthermore, [V] is the Vandermonde matrix [43] corresponding to the trilinear interpolation scheme shown in Eq. (14) and has the form

$$[V] = \begin{bmatrix} x_1x_2x_3\big|_1 & x_1x_2\big|_1 & x_1x_3\big|_1 & x_2x_3\big|_1 & x_1\big|_1 & x_2\big|_1 & x_3\big|_1 & 1 \\ x_1x_2x_3\big|_2 & x_1x_2\big|_2 & x_1x_3\big|_2 & x_2x_3\big|_2 & x_1\big|_2 & x_2\big|_2 & x_3\big|_2 & 1 \\ \vdots & \vdots & \vdots & \vdots & & & & \\ x_1x_2x_3\big|_8 & x_1x_2\big|_8 & x_1x_3\big|_8 & x_2x_3\big|_8 & x_1\big|_8 & x_2\big|_8 & x_3\big|_8 & 1 \end{bmatrix} \tag{2.12}$$

where the subscripts in the above equation are identifiers of the eight surrounding nodes. Once the coefficients are determined from Eq. (15), use of Eq. (14) at the image-point gives a final expression for the variable at the image-point of the form

$$\phi_{\text{IP}} = \sum_{i=1}^{8} \beta_i \phi_i + \text{T.E.} \tag{2.13}$$

In the above equation, $\beta$'s depend on $C$'s as well as the coordinates of the image-point. Since all of these depend only on the geometry of the immersed boundary and the grid, $\beta$'s can be determined as soon as the immersed boundary and

grid are specified. The expression for the leading order truncation error for the above interpolant has been derived in the appendix where it is shown that T.E.=$\boldsymbol{O}(\Delta^2)$ where the grid spacing is ($\boldsymbol{O}(\Delta)$). The value of variable at the ghost-cell (denoted by GC) is computed by using a linear approximation along the normal probe which incorporates the prescribed boundary condition at the boundary intercept. Thus, for Dirichlet boundary conditions that are employed for the velocity variables, the formula is

$$\phi_{BI} = \frac{1}{2}(\phi_{IP} + \phi_{GC}) + O(\Delta l^2) = \frac{1}{2}\left(\sum_{i=1}^{8} \beta_i \phi_i + \phi_G C\right) + O(\Delta^2) + O(\Delta l^2) \quad (2.14)$$

where $\Delta l$ is the length of the normal line segment extending from GC to IP. During the solution process, the above equation for the ghost-cell is written in the following implicit form

$$\phi_{GC} + \sum_{i=1}^{8} \beta_i \phi_1 = 2\phi_{BI} \quad (2.15)$$

For the pressure Poisson equation, we need to impose Neumann boundary conditions on the immersed boundary and the following second-order central-

difference, expression is written along the normal probe:

$$\begin{aligned}\left(\frac{\delta\phi}{\delta n}\right)_{BI} &= \frac{\phi_{IP}-\phi_{GC}}{\Delta l}+O(\Delta l^2)\\ &= \frac{1}{\Delta l}\left(\sum_{i=1}^{8}\beta_i\phi_i-\phi_{GC}\right)+O(\Delta^2/\Delta l)+O(\Delta l^2)\end{aligned} \tag{2.16}$$

respectively and the following implicit expression is obtained for the ghost-cell

$$\phi_{GC}-\sum_{i=1}^{8}\beta_i\phi_i=-\Delta l\left(\frac{\delta\phi}{\delta n}\right)_{BI} \tag{2.17}$$

for this boundary condition.

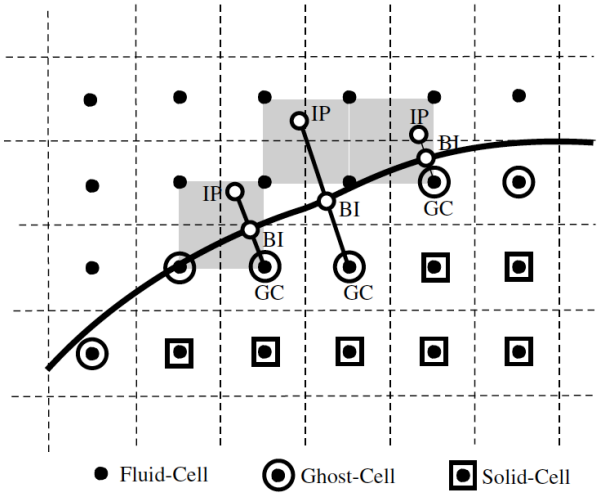


**Figure 2.2:** Schematic describing ghost-cell methodology used in the current solver. Schematic depicts an immersed boundary cutting through a Cartesian grid and identifies three particular ghost-cells (GC) that form the basis for discussion in this section. BI and IP denote boundary intercept and image-point respectively from Mittal [25].

## 2.3 Problem Setup

The two-dimensional computational model considered in the current study employs a rigid flat plate airfoil, with slightly rounded leading and trailing edges, immersed in an incompressible fluid with free-stream velocity $U_\infty$. The chord-based thickness ratio of the airfoil ($t/C$) is equal to 5%. The computational domain is $18C \times 20C$ by size, with $C$ the chord length of the flat plate. The domain is comprised of 215040 cells, with 480 points in the x-direction, and 448 in the y-direction. The geometric center of the flat plate is placed at ($10C$, $10C$) of the domain, and then it undergoes rotation about its quarter-chord, so as to achieve a series of angles of attack from 0° to 50°. A schematic of the computational domain and airfoil is shown in Fig. 2.3.

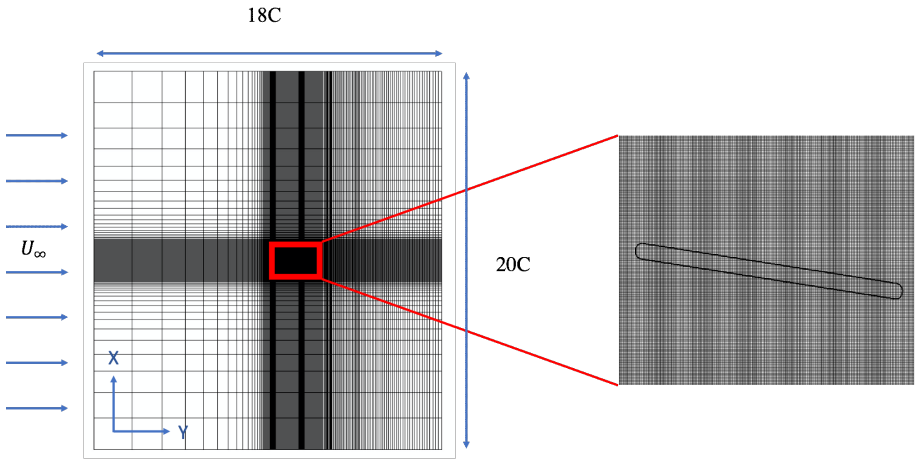


**Figure 2.3:** schematic of compuational domain and grid used for the present study.

In the x-direction, the fine mesh region around the airfoil starts from about $9.3C$ and gradually expands in the downstream direction, which ensures the

attached and shed vortices are well-resolved. In the y-direction, the fine mesh is from $9C$ to $11C$, since the relevant vortex shedding phenomenon happens and propagates mostly within this range. Such a choice of mesh is advantageous in providing accurate, yet computationally-friendly results. The grid convergence study was done by Menon and Mittal [21], and here we employ the same baseline grid as in their study. The rounding of the leading and trailing edges serves to ensure the that the flow is well resolved around those corners, and they present no significant effect on the aerodynamic characteristics and forces on the airfoil [23] In the governing incompressible Navier-Stokes equations, we define the chord-based Reynolds number as follows: $Re = \rho U_\infty C/\mu$. The reported quantities in the upcoming section are scaled using the characteristic parameters in the setup: fluid density ($\rho$), freestream velocity ($U_\infty$), and chord length ($C$), and are defined as follows:

$$C_D = F_x/(0.5\rho U_\infty^2 C^2) \tag{2.18}$$

$$C_L = F_y/(0.5\rho U_\infty^2 C^2) \tag{2.19}$$

$$C_M = M/(0.5\rho U_\infty^2 C^3) \tag{2.20}$$

Also reported are the Strouhal number of vortex shedding, $St$, and mean location of center of pressure, $X_{CP}$. As will become apparent soon, the low-$Re$

flows over the airfoil fall into one of the three categories: steady, unsteady and periodic, or unsteady and quasi-periodic. Statistical data therefore requires long integration times, especially when the time step is limited by the $CFL$ number. For all the simulations here, well-converged behavior of airfoil needs ($C/U_\infty \sim 160-280$), which translates to $3.2 \sim 5.6 \times 10^5$ time steps in our simulation. Therefore, these two-dimensional simulations require significant computational resources, and each can take up to 150 hours to run on supercomputers with multiple cores.

# Chapter 3

# Results and Discussion

## 3.1 Flow Structure at $Re = 1000$

The flow past a stationary 5% thickness flat plate at $Re = 1000$ is investigated for different angles of attack from 0° through 50°. We first begin with an overview of relevant quantities and vortex structures for some representative cases shown in Fig. 3.3. The vortex wake downstream of the flat plat airfoil transitions from steady, to a Karman vortex street, then to a leading-edge vortex (LEV) dominated flow. The major vortex patterns are categorized into different modes: 2S, 2P, 1S+1P and P for our purposes. These designations can be found in [39], where Fig. 3.1 summarizes the key characteristics for each mode of vortex shedding.

The steady state where no vortex shedding phenomenon occurs is shown by

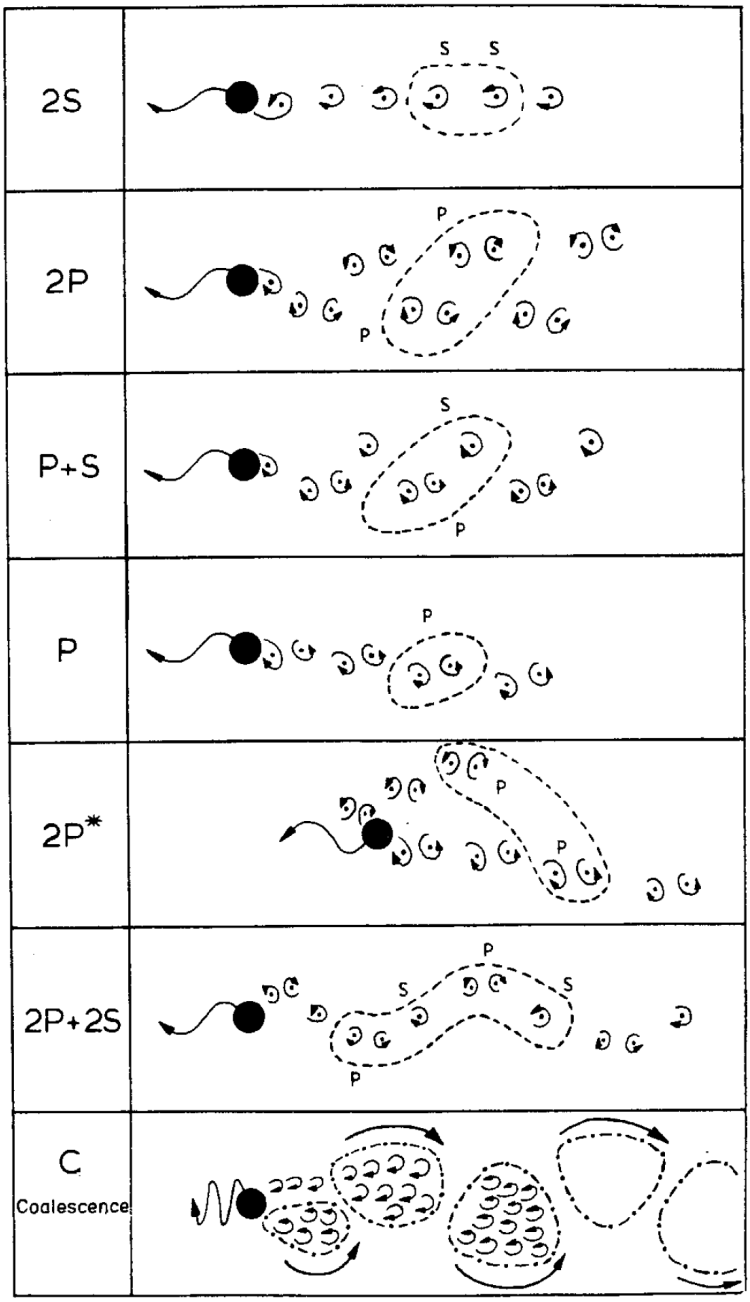


**Figure 3.1:** Sketches of the vortex shedding patterns that are found in the map in (a). "P" means a vortex pair and "S" means a single vortex, and each pattern is defined by the number of pairs and single vortices formed per cycle; - - - - encircles the vortices shed in one complete cycle from Williamson and Roshko [39].

$\alpha = 2.5°$; the steady regime extends from $\alpha = 0°$ to $\alpha = 5°$. Steady state covers the computational domain starting from about $15 \sim 20$s. The periodic Karman vortex street is observed from $\alpha = 7.5°$ until $\alpha = 15°$.

In the periodic stage, Karman vortex shedding of a single frequency component is observed. The $\alpha = 10°$ case captures the periodic oscillation of $C_L$ and $C_M$, because of Karman vortex shedding. Laminar wake instability is seen in the transient stage. The major vortex pattern here is designated as 2S, which means a vortex is fed into the downstream wake in each half cycle [39].

As $\alpha$ goes to $20° \sim 25°$, the vortex pairs starts to deviate away from the wake centerline, and convect laterally outwards [39]. There are 2 pairs of vortices being shed for each cycle, one major and one minor. This mode is characterized as the 2P mode. For $\alpha = 25°$ case, a very low frequency mode exists; the vortex structures gradually evolve from each shedding to another. The vortex structures repeat themselves about every 15 shedding cycles in a quasi-periodic manner. The shedding for this mode is dominated by both the LEV and the trailing edge vortex (TEV).

The $\alpha = 30° \sim 32.5°$ cases show the behavior where during each cycle the airfoil sheds a pair and a single vortex, called the 1S+1P mode.

When $\alpha$ is in the regime $35° \sim 50°$, the vortices is shown as one pair, or a vortex dipole, called the P mode. For $\alpha = 40°$ case, on top of the vortex pair, we see vortex mixing and separation within the computational domain. For

the $45^\circ$ case in Fig. 3.3 (**u-x**), we notice significant vortex mixing in the downstream region. The size of vortices for $45^\circ$ is larger compared to that of $30^\circ$. The LEV remain longer attached to the surface before shedding. Therefore the accumulation of LEV and TEV is more advocated; the TEV climbs to about $50\%$ chord before shedding, whereas the TEV only climb to about $30\%$ before shedding for $\alpha = 30^\circ$. When the TEV moves towards the leading edge, it pushes the LEV outward, producing the vortex shedding. At $\alpha = 50^\circ$, the size of vortices is even larger. Due to the high AOA geometry setup, the LEV is not tightly stick with the flat plate, which leads the fact that the shed vortices are more akin to circles due to this relatively high degree of freedom, instead of some evolving structures that are observed in the other AOA cases. In addition, the shedding of the TEV induces a long trail of positive vortex which later potentially merges with the corresponding TEV. The $\alpha = 50^\circ$ case induces vortices that are slow in translation motion: it takes about 13 convective time units for a particular shed vortex to form and travel 5 units of chord length , whereas it takes about 8sec for $\alpha = 30^\circ$. The large vortex size, together with the low frequency shedding, causes merge of the positive vortex from the neighboring TEVs on some occasions.

The evolution of vortex structures for $\alpha = 32.5^\circ$ and $\alpha = 35^\circ$ is shown in Fig. 3.2 (**a-e**), and (**f-j**) respactively. For $\alpha = 32.5^\circ$, the trailing edge vortex begins to accumulate and to climb towards the leading edge of the suction surface. In

the meantime, the leading edge vortex gets larger in size and convected downstream, facilitating the shedding of the TEV. The shedding is accompanied by a stream of negative vorticity, which comes form the next LEV. That stream finally evolves into two individual vortices, on either side of the flat plate. For $\alpha = 35°$, the shedding phenomenon of TEV and the convection of LEV together bring about non-linear effects at the tail of the flat plate, and the corresponding time history of force coefficients are quasii-periodic, where small changes in the vortex structures are introduced during each cycle. Such difference in shedding mode affects the mean force coefficients significantly, which will be talked about in the next section.

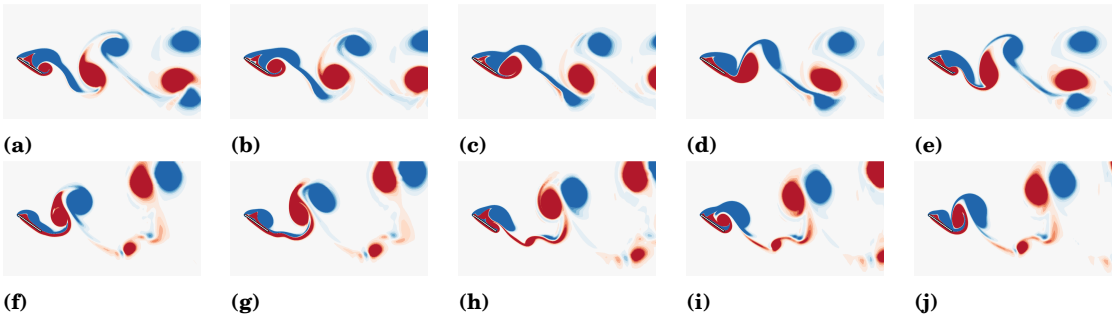


**Figure 3.2:** Snapshots of vorticity fields for unsteady behavior at $Re$ =1000. (a-e):$\alpha$ =32.5°; and(f-j): $\alpha$ =35°.

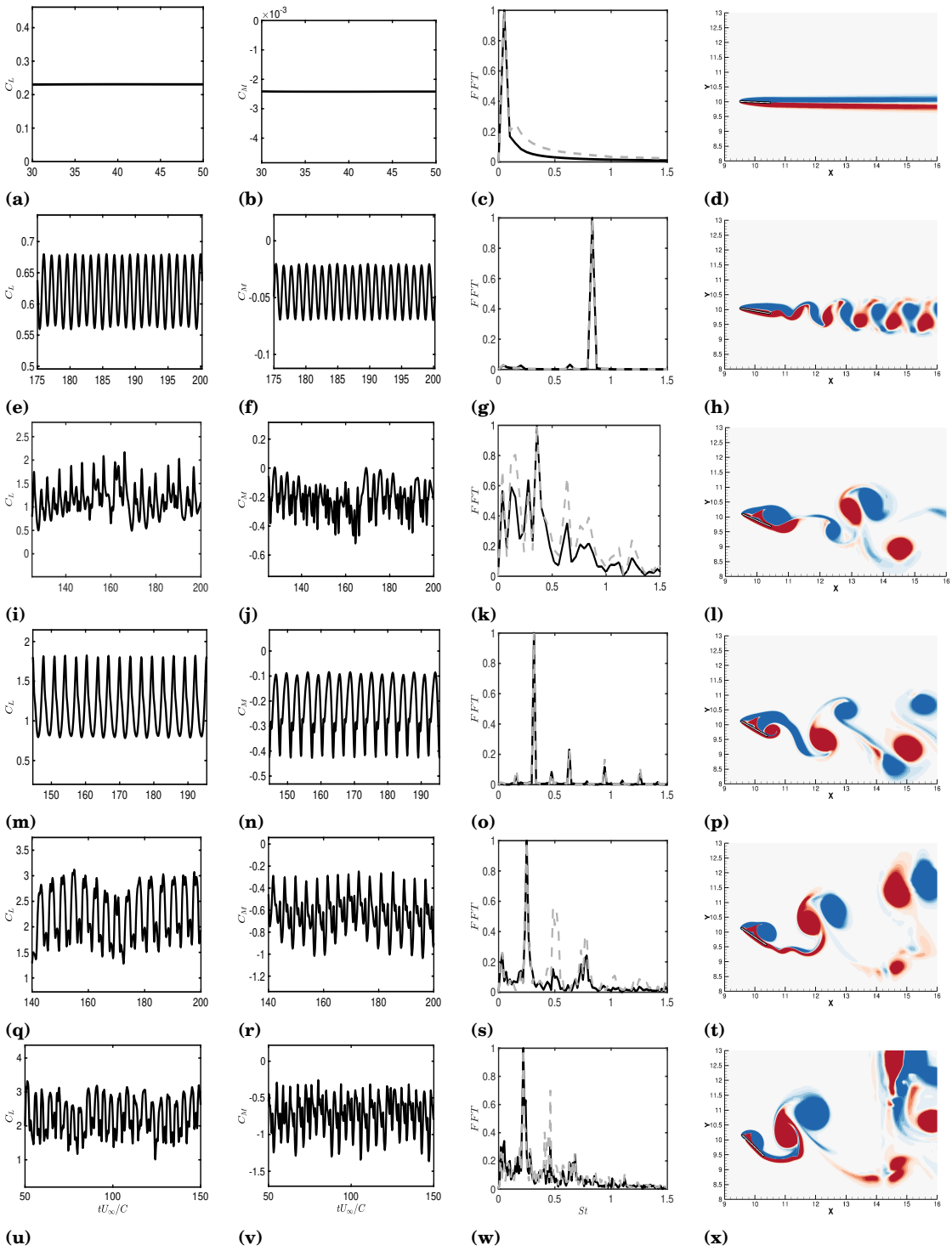


**Figure 3.3:** $C_L$(leftmost pane) and $C_M$ (middle-left pane) time history plots, frequency spectra of $C_L$ and $C_M$ (middle-right pane), and snapshots of vorticity fields (rightmost pane) for different regimes of unsteady behavior at $Re$ =1000. Frequency spectra are shown in terms of $St$, with the black and dashed gray lines showing the spectra of $C_L$ and $C_M$ normalized by each of the peak magnitude respectively. (a-d):$\alpha$ =2.5°; (e-h):$\alpha$ =10°; (i-l):$\alpha$ =25°; (m-p):$\alpha$ =30°; (q-t):$\alpha$ =35°; and (u-x):$\alpha$ =45°.

## 3.2 Force Coefficients at $Re = 1000$

The force coefficients are summarized for different $AOA$ cases. Plotted in Fig. 3.4 are the mean values of drag, lift and moment coefficients against $\alpha$. For the purpose of showing how these coefficients are spread, descriptive error bars are shown, with the upper and lower values representing one standard deviation from the mean respectively. Such choice can be found among statistical works, and marks the typical average difference between the data points with their mean [7],[8].

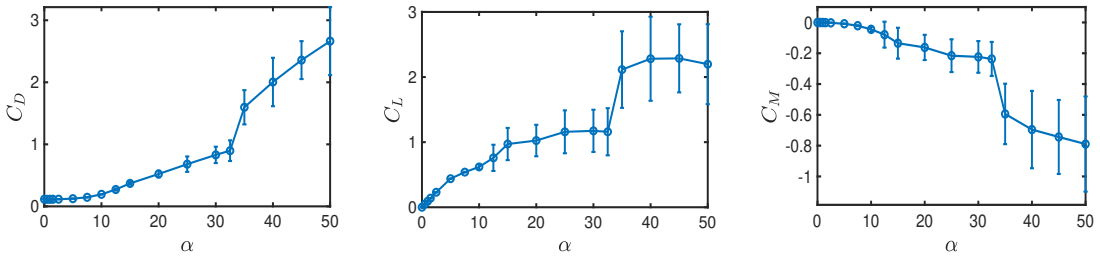


**Figure 3.4:** Force coefficients against angle of attack($\alpha$) for the present flat plate airfoil at $Re$ =1000. The bars represent one standard deviation from the mean at each angle of attack. (a) Coefficient of mean lift, $C_L$. (b) Coefficient of mean drag, $C_D$.(c) Coefficient of mean moment about quarter chord, $C_M$.

From the time series, we notice that the lift and moment coefficient plots show a variation of data sets starting from $\alpha = 7.5$. Here, we see that the drag and lift plots monotonically increases until they reach $\alpha = 32.5$, where a jump is encountered. The moment coefficient experiences a corresponding decrease over the same $AOA$ regions. After the jump, the mean of $C_D$ starts to grow with

more than twice the original slope:

$$m_1 = \Delta C_D/\Delta\alpha = (C_{D,\alpha_1=32.5} - C_{D,\alpha_2=7.5})/(\alpha_1 - \alpha_2) = 0.0301, \tag{3.1}$$

$$m_2 = \Delta C_D/\Delta\alpha = (C_{D,\alpha_3=50} - C_{D,\alpha_4=35})/(\alpha_3 - \alpha_4) = 0.0711, \tag{3.2}$$

$$m_2/m_1 = 2.3621; \tag{3.3}$$

$C_L$ stays roughly unchanged whereas $C_M$ starts to decrease about 1.5 times the slope:

$$m_3 = \Delta C_M/\Delta\alpha = (C_{M,\alpha_1=32.5} - C_{M,\alpha_2=7.5})/(\alpha_1 - \alpha_2) = -0.0086, \tag{3.4}$$

$$m_4 = \Delta C_M/\Delta\alpha = (C_{M,\alpha_3=50} - C_{M,\alpha_4=35})/(\alpha_3 - \alpha_4) = -0.0130, \tag{3.5}$$

$$m_4/m_3 = 1.5116. \tag{3.6}$$

With increasing $\alpha$, we also see larger spread of the data, especially after the jump. We can refer to the discussion in the previous section, where symbolic designations of the vortices are assigned. In particular, the designation just prior to the threshold is periodic 1S-1P, whereas that afterwards becomes quasi-periodic P. Such shift in vortex modes causes the markedly different behavior in the force coefficients plots, in both its linear trend and standard deviation bounds. In an attempt to testify whether the simulation data is reliable,

we first compare with Menon's work [21], where the same computational domain and methods are employed:

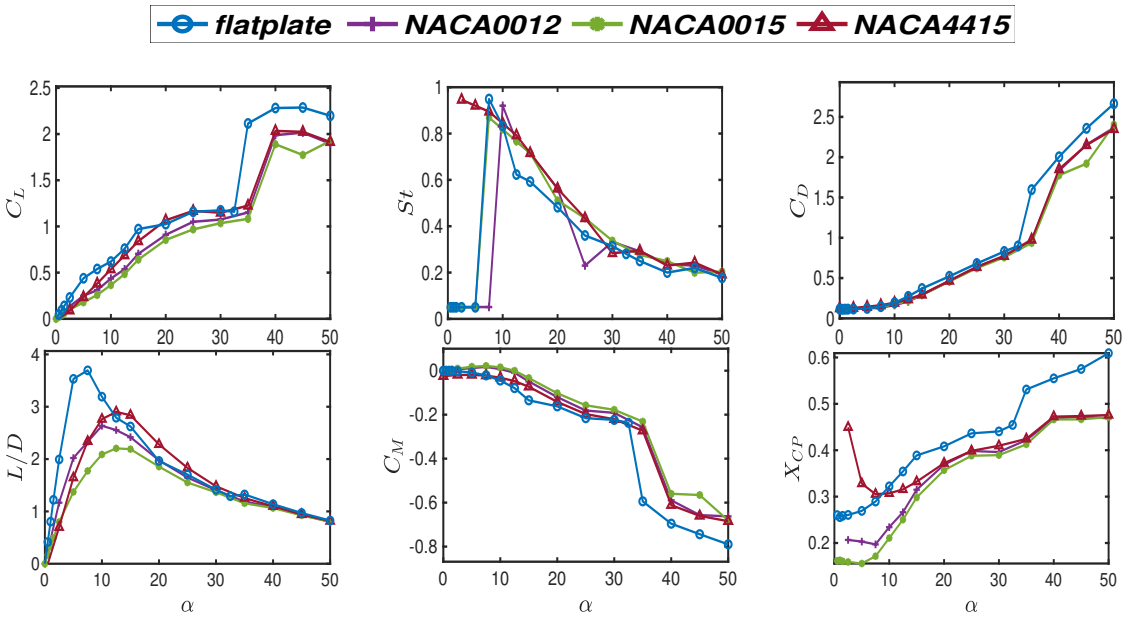


**Figure 3.5:** Force coefficients against angle of attack($\alpha$) for the flat plate airfoil at $Re$ =1000, compared to the three airfoil shapes from Menon [21]. (a) Coefficient of mean lift, $C_L$. (b) Strouhal number, $St$, of $C_L$ oscillations. (c) Coefficient of mean drag, $C_D$. (d) Lift-to-drag ratio. (e) Coefficient of mean moment about quarter chord, $C_M$. (f) Mean location of center of pressure, $X_{CP}$.

We notice that the effect of different shapes of the airfoil of his data is observable but small. However their discrepancies with the current flat plate airfoil case is remarkably large. The drag, lift and moment plots generally follow the trend of the other airfoil shapes, but the jump in the relevant parameters was found to be several degrees left along the $\alpha$-axis. For the $L/D$ plot, the maximum for the flat plate is observed at $\alpha = 7.5°$, and the corresponding value is at least a $27\%$ increase compared to the peaks of other airfoil shapes. It attains a $67\%$ increase in $L/D$ compared to the maximum for the NACA 0015 airfoil. This enormous increase provides strong basis that the flat plate airfoil

is the most efficient airfoil shape at this $Re$ number, and its performance is better than those conventional airfoil shapes. The center of pressure is found to have a $5\% \sim 15\%$ increase from other airfoil shape, as a consequence of the lower values of $C_M$, especially at the tails.

Winslow *et al.* [40] in their work show at a certain $AOA$, lift is taken over by a lower $Re$ for the NACA 0012 airfoil, which occurs at about $15°$ for the relevant $Re$ number. Higher $Re$ also carries lower drag for almost all $AOA$s in Fig. 3.6.

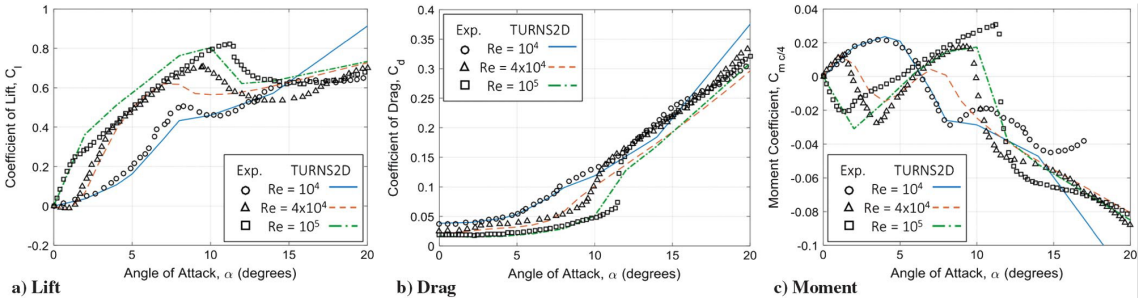


**Figure 3.6:** Lift, drag, and pitching moment comparison of CFD predictions for NACA 0012 between Reynolds numbers of $10^4$ and $10^5$ from Winslow [40]

A similar trend is also observable in the newly generated plot, Fig. 3.7, where the data from current research is juxtaposed with flat plates of various thickness at a higher $Re$ number.

The $C_L$ and $C_D$ plots are obtained by adding the results from [29], where the data sets represent a $5\%$, $3\%$ or $1\%$ chord-based thickness respectively, for a $Re$ number of $10^4$. At that particular $Re$ number, we notice an small increase in lift aft about $7°$ without a significant change in drag profile when the thickness of the plate is increased for an $AOA$ up to $20°$. Current data suggests that a takeover of lift occurs at about $12.5°$. The drag is closest to the high Re profile

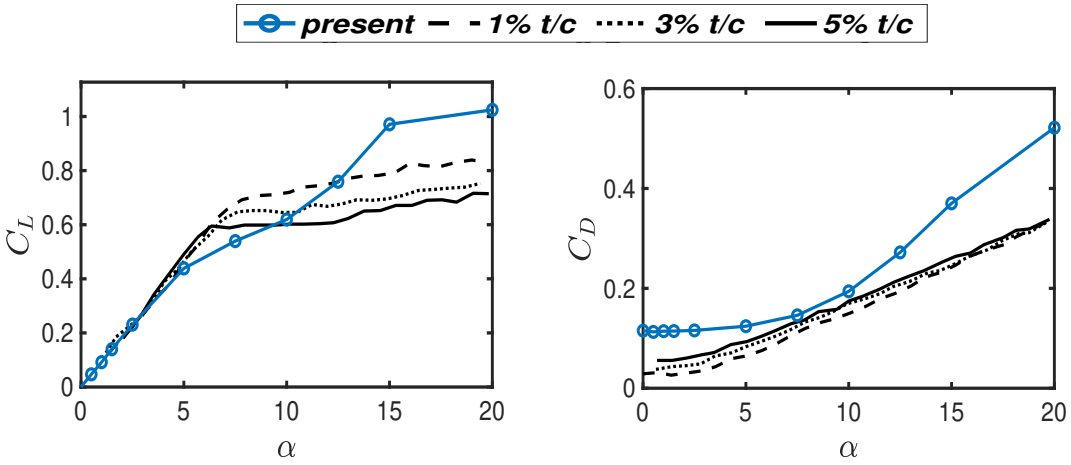


**Figure 3.7:** Force coefficients against angle of attack($\alpha$) for the flat plate airfoil at $Re$ =1000, compared to the plate airfoils of different thickness at $Re$ =$10^4$ from Winslow *et al.* [40]. (a) Coefficient of mean lift, $C_L$. (b) Coefficient of mean drag, $C_D$.

at about $7.5°$. Away from that point, the drag is much higher, and it better fits a polynomial trending, rather than a rectilinear one, as is the case for $Re = 10^4$. Now that the results are in good agreement in both its shear values and overall trend, compared to different literature, we can extend the discussion to other $Re$ numbers.

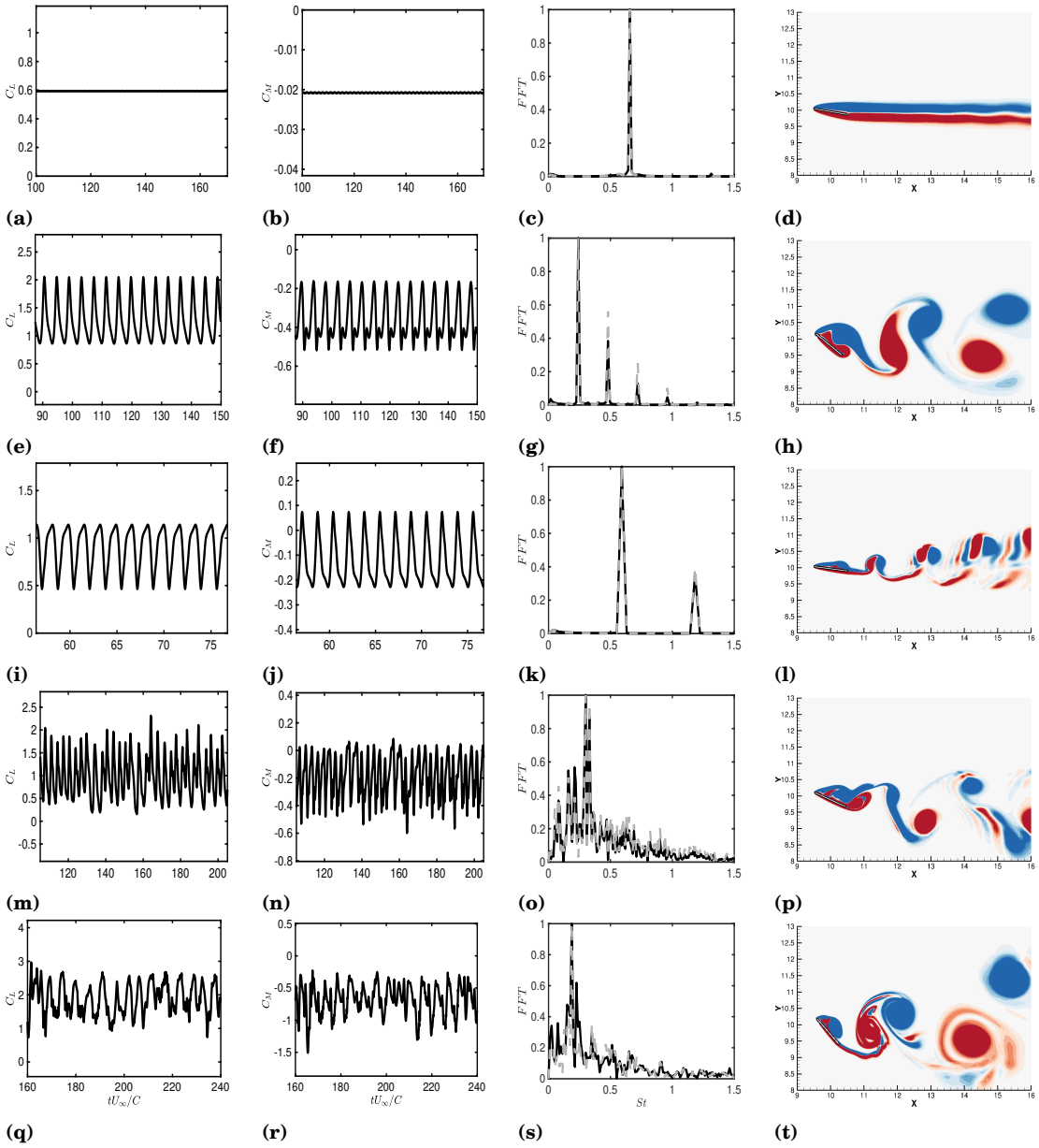


**Figure 3.8:** $C_L$(leftmost pane) and $C_M$ (middle-left pane) time history plots, frequency spectra of $C_L$ and $C_M$ (middle-right pane), and snapshots of vorticity fields (rightmost pane) for different regimes of unsteady behavior at $Re$ =500 and 2000. Frequency spectra are shown in terms of $St$, with the black and dashed gray lines showing the spectra of $C_L$ and $C_M$ normalized by each of the peak magnitude respectively. (a-d):$Re$ =500, $\alpha$ =10°; (e-h):$Re$ =500, $\alpha$ =20°; (i-l):$Re$ =500, $\alpha$ =40°; (m-p):$Re$ =2000, $\alpha$ =7.5°; (q-t):$Re$ =2000, $\alpha$ =25°; and (u-x):$Re$ =2000, $\alpha$ =50°.

## 3.3 Effects of Reynolds Number

To investigate the effects of $Re$ number, additional simulations are performed at $Re = 500$ and $2000$. The results are summarized in Figs. 3.8, 3.9, 3.10, 3.11, 3.12, and 3.13.

### 3.3.1 Flow Structures

Due to the nonlinear effects of the convective term, the transition of flow structures, as shown in Fig. 3.8, is found to be extremely different for different $Re$ numbers. For $Re = 500$ in particular, flow structure starts with steady state with no vortex shedding, and laminar wake instability where vortex shedding occurs further downstream beyond the computational domain. The symbolic designations start from $\alpha = 12.5°$ with periodic Karman vortex shedding, or 2S. As $\alpha$ is above $35°$, the designation becomes the P mode. For $Re = 2000$, the transition of modes follows the order of 2S, 1S+1P, 2P and finally P as the $AOA$ increases. Because of the relatively high $Re$ number, the vortex structures are hard to be distinguished as one mode at times and might fall into one of the two modes, depending on how much weight is assigned to the minor vortex. At $\alpha = 40°$, LEV reattachment phenomenon is observed.

### 3.3.2 Force Coefficients

The force coefficients plots are summarized in Figs. 3.9, 3.10, 3.11, 3.12, and 3.13. Similar to the situation for $Re = 1000$, we notice a universally better performance ($L/D$) for the flat plate airfoil over traditional shapes across all $Re$ numbers.

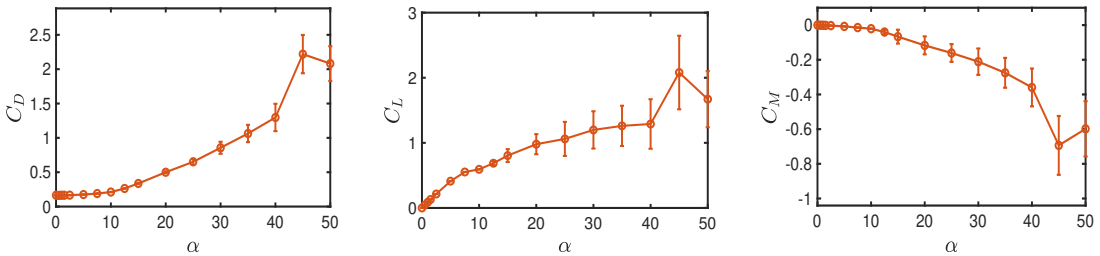


**Figure 3.9:** Force coefficients against angle of attack($\alpha$) for the flat plate airfoil at $Re$ =500. The bars represent one standard deviation from the mean at each angle of attack. (a) Coefficient of mean lift, $C_L$. (b) Coefficient of mean drag, $C_D$.(c) Coefficient of mean moment about quarter chord, $C_M$.

In Fig. 3.9, descriptive bars are plotted for $Re = 500$ against the $AOA$s. The fluctuations of the force coefficients are closer to the mean values, compared to the $Re = 1000$ cases. The maximum fluctuations for $Re = 500$ are around $15.3\%$, $29.5\%$, and $59.8\%$ for $C_D$, $C_L$, and $C_M$ respectively, whereas the corresponding values for $Re = 1000$ are $20.6\%$, $31.3\%$, and $106\%$. The overall trend is an increase of drag and lift coefficients, with a decrease at $\alpha = 50°$. The maximum values for $C_D$, $C_L$ are slightly lower. The opposite is true for the moment coefficient. Fig. 3.10 shows comparison of the flat plate with the NACA 0015 airfoil at $Re = 500$. The increase in lift forces is up to $86.4\%$, observed at $\alpha = 5°$. The drag forces, expect at $\alpha = 45°$, are within $20\%$ from the NACA 0015 airfoil. The

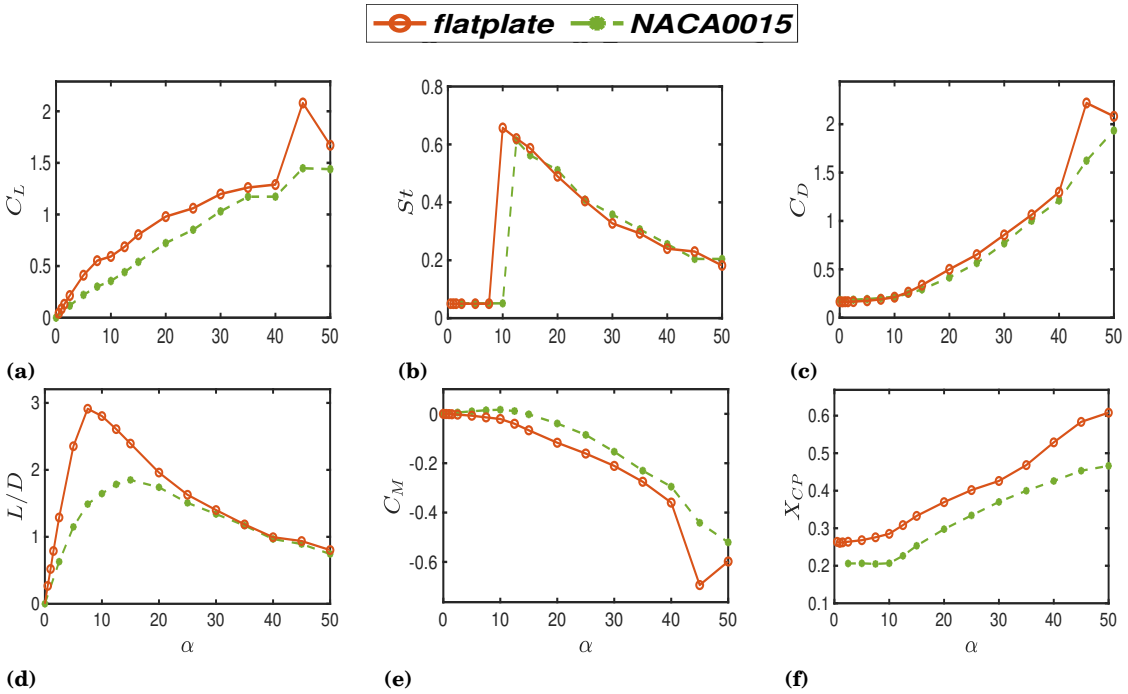


**Figure 3.10:** Force coefficients against angle of attack($\alpha$) for the flat plate airfoil at $Re$ =500, compared to the NACA 0015 airfoil from Menon [21]. (a) Coefficient of mean lift, $C_L$. (b) Strouhal number, $St$, of $C_L$ oscillations. (c) Coefficient of mean drag, $C_D$. (d) Lift-to-drag ratio. (e) Coefficient of mean moment about quarter chord, $C_M$. (f) Mean location of center of pressure, $X_{CP}$.

resulting aerodynamic performance, $L/D$, is therefore enhanced by up to $105\%$, where the maximum occurs at $\alpha = 5°$.

In Fig. 3.11, descriptive bars are plotted for $Re = 2000$ against the $AOA$s. Drag and lift coefficients are more spread from their means, compared to the $Re = 1000$ cases. The maximum fluctuations for $Re = 2000$ are around $28.6\%$, $47.4\%$, and $81.3\%$ for $C_D$, $C_L$, and $C_M$ respectively. The overall trend is still a monotonic increase in drag, whereas the lift experiences a mild stall from $15° \sim 25°$, followed by a jump to over 2 and generally stays there, with a mild decrease at its tail. The moment coefficient is similar to the lift coefficient except with the sign flipped. Fig. 3.12 shows comparison of the flat plate with

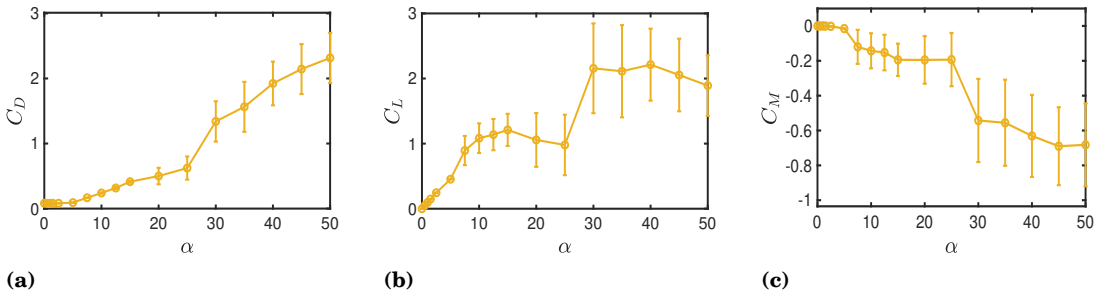


**(a)** **(b)** **(c)**

**Figure 3.11:** Force coefficients against angle of attack($\alpha$) for the flat plate airfoil at $Re$ =2000. The bars represent one standard deviation from the mean at each angle of attack. (a) Coefficient of mean lift, $C_L$. (b) Coefficient of mean drag, $C_D$.(c) Coefficient of mean moment about quarter chord, $C_M$.

the NACA 0015 airfoil at $Re = 2000$. The increase in lift is up to $221\%$, observed at $\alpha = 7.5°$. The drag profile are within $47.5\%$ from the NACA 0015 airfoil, expect for the jump point. Overall, the resulting aerodynamic performance, $L/D$ is enhanced by up to $216\%$, where the maximum is located at $\alpha = 5°$ as well. In addition, the initiation of vortex shedding, which happens at $\alpha = 7.5°$, is at a much lower frequency, compared to the NACA 0015 airfoil, although they gradually converge as $AOA$ increases.

Plotted in Fig. 3.13 are the three $Re$ number cases for the flat plate airfoil, against the angle of attack. The mean $C_D$ shows a monotonic increase across the $AOA$s, but the values are not quite different for different $Re$ numbers. The mean $C_L$ are higher for higher $Re$ numbers momentarily before and after the jumps; at both tails; however, the values are closer together. A higher $Re$ number seems to promote the jump in the lower $\alpha$ direction. The jump is apparent for $C_L$, $C_D$, and $C_M$ profiles. The lift for $Re = 500$ and $1000$ lack the deep stall region, which is observable for high-$Re$ cases. However, there is a mild stall

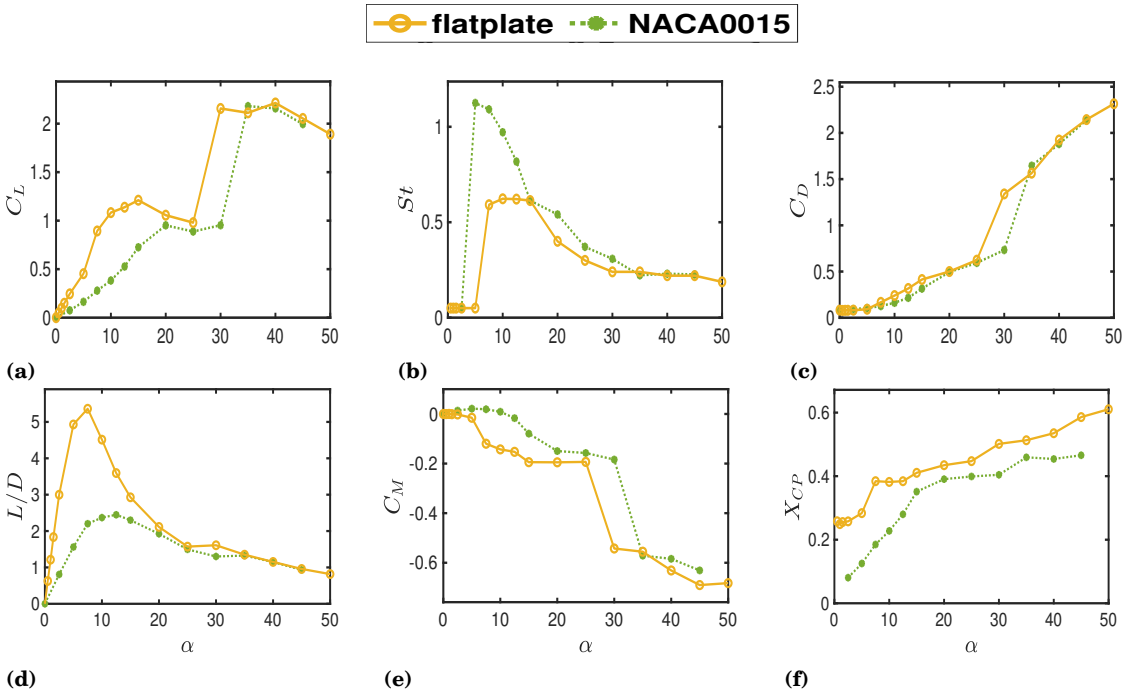


**Figure 3.12:** Force coefficients against angle of attack($\alpha$) for the flat plate airfoil at $Re$ =2000, compared to the NACA 0015 airfoil from Menon [21]. (a) Coefficient of mean lift, $C_L$. (b) Strouhal number, $St$, of $C_L$ oscillations. (c) Coefficient of mean drag, $C_D$. (d) Lift-to-drag ratio. (e) Coefficient of mean moment about quarter chord, $C_M$. (f) Mean location of center of pressure, $X_{CP}$.

apparent for $Re = 2000$ flat plate case. Higher $Re$ number leads to better aerodynamic performance, in agreement with numerous studies on the effect of $Re$ number on airfoils [12], [27]. In general, the aerodynamic performance for the flat plate is much better compared to the NACA 0015 airfoil at $Re = 500$, $1000$ and $2000$ respectively, shown in the previous discussion. For the flat plate airfoil alone, $L/D$ is enhanced by over $109\%$ for $Re = 2000$, compared to $Re = 500$ at $\alpha = 5°$.

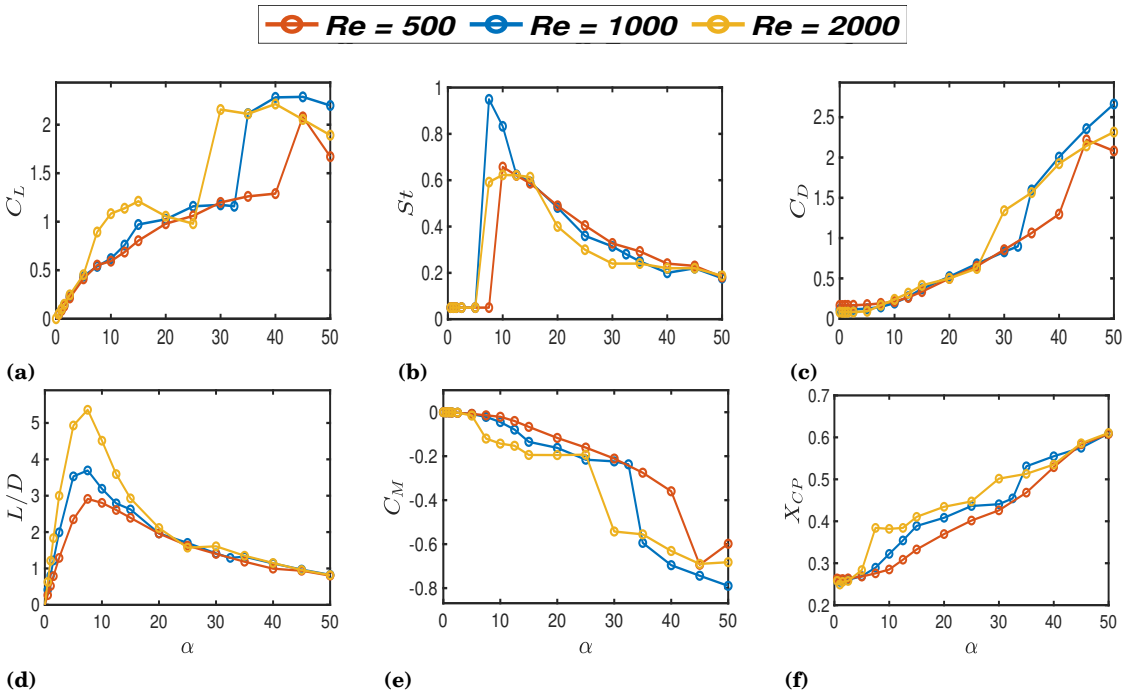


**Figure 3.13:** Force coefficients against angle of attack($\alpha$) for the flat plate airfoil at $Re$ =500, 1000, and 2000. (a) Coefficient of mean lift, $C_L$. (b) Strouhal number, $St$, of $C_L$ oscillations. (c) Coefficient of mean drag, $C_D$. (d) Lift-to-drag ratio. (e) Coefficient of mean moment about quarter chord, $C_M$. (f) Mean location of center of pressure, $X_{CP}$.

# Chapter 4

# Conclusion

A study of the aerodynamic characteristics of 5% thin flat plate airfoil at ultra low $Re$ numbers has been carried out using a Navier-Stokes solver. The aims of this research are twofold: first to investigate if a flat plate shape is aerodynamically efficient compared to other shapes, and second to provide a data base of the aerodynamic coefficients for different Re numbers. It is shown that the flow structures for different cases can be categorized into different designations, including 2S, 2P, 1S+1P and P. In addition, the force coefficients plots demonstrate that the flat plate is the able to greatly enhance lift while keeping the drag at comparable values to other airfoil shapes. This finding provides evidence that the flat plate is the most aerodynamically efficient shape across all the Reynolds numbers ranged from 500 to 2000 investigated in this study. Its performance is better as the Reynolds number increases. The current study in-

herits several aspects of limitations. First, the simulations are performed with two-dimensional modelling. This does not inform us about how fluid structures would be affected by the introduction of the three-dimensional effects, such as tip vorticies and streamwise vortex roll-up. The current study also does not utilize different thicknesses. Therefore it would be worth investigating the effect of thickness and camber in the future.

# Bibliography


[1] I.H. Abbott and V.A. E. Doenhoff. *Theory of Wing Sections: Including a Summary of Airfoil Data (Dover Books on Aeronautical Engineering)*. Dover Publications, 1959.

[2] S AHUJA and CW ROWLEY. "Feedback control of unstable steady states of flow past a flat plate using reduced-order estimators". In: *Journal of Fluid Mechanics* 645 (2010), pp. 447–478. DOI: 10.1017/s0022112009992655.

[3] D. Anderson et al. *Computational Fluid Mechanics and Heat Transfer (Computational and Physical Processes in Mechanics and Thermal Sciences)*. 4th ed. CRC Press, 2020.

[4] M Bozkurttas et al. "Towards Numerical Simulation of Flapping Foils on Fixed Cartesian Grids". In: *43rd AIAA Aerospace Sciences Meeting and Exhibit* (2005). DOI: 10.2514/6.2005-79.

[5] B. Carmichael. *Low Reynolds number airfoil survey, volume 1 — Semantic Scholar*. 1981. URL: https://www.semanticscholar.org/paper/

Low-Reynolds-number-airfoil-survey%5C%2C-volume-1-Carmichael/3ee1714d8c461439f0a5dd51171051606c5e6651.

[6] R CARMICHAEL and L ERICKSON. "PAN AIR - A higher order panel method for predicting subsonic or supersonic linear potential flows about arbitrary configurations". In: *14th Fluid and Plasma Dynamics Conference* (1981). DOI: 10.2514/6.1981-1255.

[7] G Cumming, J Williams, and F Fidler. "Replication and Researchers' Understanding of Confidence Intervals and Standard Error Bars". In: *Understanding Statistics* 3.4 (2004), pp. 299–311. DOI: 10.1207/s15328031us0304_5.

[8] G Cumming et al. "Statistical Reform in Psychology". In: *Psychological Science* 18.3 (2007), pp. 230–232. DOI: 10.1111/j.1467-9280.2007.01881.x.

[9] FN Felten and TS Lund. "Kinetic energy conservation issues associated with the collocated mesh scheme for incompressible flow". In: *Journal of Computational Physics* 215.2 (2006), pp. 465–484. DOI: 10.1016/j.jcp.2005.11.009.

[10] Y HOARAU et al. "Organized modes and the three-dimensional transition to turbulence in the incompressible flow around a NACA0012 wing".

In: *Journal of Fluid Mechanics* 496 (2003), pp. 63–72. DOI: 10.1017/s0022112003006530.

[11] J. C. R. Hunt, A. A. Wray, and P. Moin. *Eddies, streams, and convergence zones in turbulent flows*. Dec. 1, 1988. URL: https://ntrs.nasa.gov/citations/19890015184.

[12] S Jain, N Sitaram, and S Krishnaswamy. "Effect of Reynolds Number on Aerodynamics of Airfoil with Gurney Flap". In: *International Journal of Rotating Machinery* 2015 (2015), pp. 1–10. DOI: 10.1155/2015/628632.

[13] P Kunz and I Kroo. "Analysis and Design of Airfoils for Use at Ultra-Low Reynolds Numbers". In: *Fixed and Flapping Wing Aerodynamics for Micro Air Vehicle Applications* (2001), pp. 35–60. DOI: 10.2514/5.9781600866654.0035.0060.

[14] P Kunz, I Kroo, and J Alonso. *Analysis , Design , and Testing of Airfoils for Use at Ultra-Low Reynolds Numbers — Semantic Scholar*. 2004. URL: https://www.semanticscholar.org/paper/Analysis-%5C%2C-Design-%5C%2C-and-Testing-of-Airfoils-for-Use-Kroo/7bb774db8c5ecc1ac35914ba131af21e2199297e.

[15] DF Kurtulus. "On the Unsteady Behavior of the Flow around NACA 0012 Airfoil with Steady External Conditions at Re=1000". In: *International*

*Journal of Micro Air Vehicles* 7.3 (2015), pp. 301–326. DOI: 10.1260/1756-8293.7.3.301.

[16] JCM Lin and LL Pauley. "Low-Reynolds-number separation on an airfoil". In: *AIAA Journal* 34.8 (1996), pp. 1570–1577. DOI: 10.2514/3.13273.

[17] PBS Lissaman. "Low-Reynolds-Number Airfoils". In: *Annual Review of Fluid Mechanics* 15.1 (1983), pp. 223–239. DOI: 10.1146/annurev.fl.15.010183.001255.

[18] Y Liu et al. "Numerical bifurcation analysis of static stall of airfoil and dynamic stall under unsteady perturbation". In: *Communications in Nonlinear Science and Numerical Simulation* 17.8 (2012), pp. 3427–3434. DOI: 10.1016/j.cnsns.2011.12.007.

[19] D Mavriplis and V Venkatakrishnan. "A 3D agglomeration multigrid solver for the Reynolds-averaged Navier-Stokes equations on unstructured meshes". In: *33rd Aerospace Sciences Meeting and Exhibit* (1995). DOI: 10.2514/6.1995-345.

[20] S.F. McCormick. *Multigrid Methods*. Society for Industrial and Applied Mathematics, 1987.

[21] K Menon and R Mittal. “Aerodynamic Characteristics of Canonical Airfoils at Low Reynolds Numbers”. In: *AIAA Journal* 58.2 (2020), pp. 977–980. DOI: 10.2514/1.j058969.

[22] K Menon and R Mittal. “Computational Modelling and Analysis of Aeroelastic Flutter”. In: *2018 Fluid Dynamics Conference* (2018). DOI: 10.2514/6.2018-3080.

[23] K Menon and R Mittal. “Flow physics and dynamics of flow-induced pitch oscillations of an airfoil”. In: *Journal of Fluid Mechanics* 877 (2019), pp. 582–613. DOI: 10.1017/jfm.2019.627.

[24] S.J. Miley. *A catalog of low Reynolds number airfoil data for wind turbine applications*. National Technical Information Service, U.S. Dept. of Commerce, 1982.

[25] R Mittal et al. “A versatile sharp interface immersed boundary method for incompressible flows with complex boundaries”. In: *Journal of Computational Physics* 227.10 (2008), pp. 4825–4852. DOI: 10.1016/j.jcp.2008.01.028.

[26] S Mittal and T Tezduyar. “Massively parallel finite element computation of incompressible flows involving fluid-body interactions”. In: *Computer Methods in Applied Mechanics and Engineering* 112.1-4 (1994), pp. 253–282. DOI: 10.1016/0045-7825(94)90029-9.

[27] TJ Mueller and SM Batill. “Experimental Studies of Separation on a Two-Dimensional Airfoil at Low Reynolds Numbers”. In: *AIAA Journal* 20.4 (1982), pp. 457–463. DOI: 10.2514/3.51095.

[28] K Ohmi et al. “Vortex formation around an oscillating and translating airfoil at large incidences”. In: *Journal of Fluid Mechanics* 211 (1990), pp. 37–60. DOI: 10.1017/s0022112090001483.

[29] M Okamoto, K Yasuda, and A Azuma. “Aerodynamic characteristics of the wings and body of a dragonfly”. In: *Journal of Experimental Biology* 199.2 (1996), pp. 281–294. DOI: 10.1242/jeb.199.2.281.

[30] CL Perrin. “Numerical Recipes in Fortran 90: The Art of Scientific Computing, Second Edition, Volume 2 (3 CD-ROMs and Manual) By William H. Press, Saul A. Teukolsky, William T. Vetterling, and Brian P. Flannery. Cambridge University Press: New York, 1996.” In: *Journal of the American Chemical Society* 119.37 (1997), pp. 8748–8748. DOI: 10.1021/ja965936f.

[31] DJ Pines and F Bohorquez. “Challenges Facing Future Micro-Air-Vehicle Development”. In: *Journal of Aircraft* 43.2 (2006), pp. 290–305. DOI: 10.2514/1.4922.

[32] JH Seo and R Mittal. “A sharp-interface immersed boundary method with improved mass conservation and reduced spurious pressure oscil-

lations". In: *Journal of Computational Physics* 230.19 (2011), pp. 7347–7363. DOI: 10.1016/j.jcp.2011.06.003.

[33] JH Seo et al. "Flow physics of normal and abnormal bioprosthetic aortic valves". In: *International Journal of Heat and Fluid Flow* 86 (2020), p. 108740. DOI: 10.1016/j.ijheatfluidflow.2020.108740.

[34] K Stüben. "A review of algebraic multigrid". In: *Journal of Computational and Applied Mathematics* 128.1-2 (2001), pp. 281–309. DOI: 10.1016/s0377-0427(00)00516-1.

[35] K TAIRA and T COLONIUS. "Three-dimensional flows around low-aspect-ratio flat-plate wings at low Reynolds numbers". In: *Journal of Fluid Mechanics* 623 (2009), pp. 187–207. DOI: 10.1017/s0022112008005314.

[36] J Tank, L Smith, and GR Spedding. "On the possibility (or lack thereof) of agreement between experiment and computation of flows over wings at moderate Reynolds number". In: *Interface Focus* 7.1 (2017), p. 20160076. DOI: 10.1098/rsfs.2016.0076.

[37] H Udaykumar et al. "A Sharp Interface Cartesian Grid Method for Simulating Flows with Complex Moving Boundaries". In: *Journal of Computational Physics* 174.1 (2001), pp. 345–380. DOI: 10.1006/jcph.2001.6916.

[38] J van Kan. “A Second-Order Accurate Pressure-Correction Scheme for Viscous Incompressible Flow”. In: *SIAM Journal on Scientific and Statistical Computing* 7.3 (1986), pp. 870–891. DOI: 10.1137/0907059.

[39] C Williamson and A Roshko. “Vortex formation in the wake of an oscillating cylinder”. In: *Journal of Fluids and Structures* 2.4 (1988), pp. 355–381. DOI: 10.1016/s0889-9746(88)90058-8.

[40] J Winslow et al. “Basic Understanding of Airfoil Characteristics at Low Reynolds Numbers (104–105)”. In: *Journal of Aircraft* 55.3 (2018), pp. 1050–1061. DOI: 10.2514/1.c034415.

[41] T Ye et al. “An Accurate Cartesian Grid Method for Viscous Incompressible Flows with Complex Immersed Boundaries”. In: *Journal of Computational Physics* 156.2 (1999), pp. 209–240. DOI: 10.1006/jcph.1999.6356.

[42] Y Zang, RL Street, and JR Koseff. “A Non-staggered Grid, Fractional Step Method for Time-Dependent Incompressible Navier-Stokes Equations in Curvilinear Coordinates”. In: *Journal of Computational Physics* 114.1 (1994), pp. 18–33. DOI: 10.1006/jcph.1994.1146.